Int. J. Heat Mass Transfer. Vol. 35, No. 1, pp. 175–186, 1992
Printed in Great Britain

0017–9310/92 $5.00 + 0.00

Natural convection in porous media—I. Nonfreezing

H. LEIN and RICHARD S. TANKIN
Department of Mechanical Engineering, Northwestern University, Evanston, IL 60201, U.S.A.

(*Received* 15 *February* 1990 *and in final form* 27 *December* 1990)

Abstract—The Christiansen filter concept is used to visualize natural convection in porous media. Studies are conducted with both permeable and impermeable upper boundaries. The experimental results agree well with the numerical calculations which are based upon Darcy's law. Three different permeabilities as well as different test section aspect ratios (width/height) are examined. It is found that the aspect ratio of the cells does not vary with modified Rayleigh number for the impermeable upper boundary but this ratio increases significantly with modified Rayleigh number for the permeable upper boundary.

INTRODUCTION

In recent years, because of its increase in importance in many technological processes, a great deal of interest has focused on natural convection in a porous medium. For example, natural convection in a porous medium is intrinsically related to geothermal energy sources, long term storage of solar energy in aquifers, porous medium insulation in the walls and roofs of buildings, enhanced recovery of oil, etc. Since 1970 there have been many studies—primarily theoretical or numerical—on natural convection in porous media in which new analytical techniques were employed. Holst and Aziz [1] used a pseudo-stream function to analyze the set of governing differential equations, and developed a numerical algorithm which included the temperature dependence on the physical properties. The effects of variable permeability and upper surface confinement were studied by Ribando and Torrance [2]. As for the experimental studies, several investigators such as Holst and Aziz [1], and Bau and Torrance [3], used thermistor probes or thermocouples to measure local temperatures and thus determined such quantities as wavelength of the cells, isotherm profiles, etc. These probes locally disturb the porosity where the measurements are being made; and although these measurements may agree with their numerical results, they are suspect. In addition, there is no way to ensure their two-dimensional flow field assumption is valid. Klarsfeld [4] used an optical technique based on the Christiansen filter concept to visualize the temperature profile of a porous medium under natural convection. Excellent reviews of convection in porous media are contained in the works of Combarnous and Bories [5] and Bejan [6].

The experiments reported in this paper are based on the Christiansen filter concept. The index of refraction of a fluid is a function of both its temperature and the wavelength of the incident light; whereas, the index of refraction of the solid (glass) is primarily a function of the wavelength of the incident light and only very weakly a function of temperature. Thus, if a temperature gradient exists in the porous medium which is perpendicular to the optical axis (of the incident light), various wavelengths of light will penetrate the test section at different locations. This situation arises because the indices of refraction of the fluid and the solid medium match at one wavelength for a particular temperature. For this system to operate properly, the flow must be two-dimensional and the index of refraction (of the liquid and solid) must match over the temperature range under consideration. Of course, the fluid and the solid must be transparent to the light source. It is important to stress that the flow must be two-dimensional and aligned with the optical axis, otherwise the incident light will not penetrate the test section. This experimental technique used by Klarsfeld has been extended by using a dye laser instead of a Cd–Hg arc lamp. A laser light source has a much greater intensity than a Cd–Hg arc lamp, is much more monochromatic and is essentially a parallel beam of light. All of these characteristics are important. A digital camera is used to digitize the signals and a software package called 'image processor' is used to further clearly delineate the output signal. Thus improvements in using the Christiansen filter technique are expected.

This study is divided into two parts: Part I deals with convection in a porous medium consisting of a liquid phase and glass beads, and Part II deals with a porous medium where a phase change occurs in the liquid phase.

EXPERIMENTAL SETUP

The test section (see Fig. 1(a)) in which the experiments were conducted is similar to the one used in ref. [7] for Bénard cell studies; but with some important modifications—the size and materials of the test section and windows were changed. The dimensions of

NOMENCLATURE

C_p	specific heat [kJ kg^{-1} °C^{-1}]
$f(T)$	viscosity non-dimensionalization factor
g	gravitational constant [m s^{-2}]
H	height of the test section [m]
K	permeability [m^2]
k, k_m	thermal conductivity [W m^{-1} °C^{-1}]
L	width of the test section [m]
n_l, n_s	index of refraction
Nu	Nusselt number
P	pressure in the porous medium [N m^{-2}]
Ra	Rayleigh number, $Kg\beta\Delta TH/\nu\alpha$
t	time [s]
T	temperature [°C]
U	area averaged horizontal velocity [m s^{-1}]
V	area averaged vertical velocity [m s^{-1}]
X	horizontal Cartesian coordinate
Y	vertical Cartesian coordinate.

Greek symbols

α	thermal diffusivity [m^2 s^{-1}]
β	thermal expansion coefficient
λ	wavelength [Å]
μ	viscosity
ν, ν_0	kinematic viscosity [m s^{-2}]
ρ, ρ_0	density [kg m^{-3}]
ψ	stream function.

Superscripts

(i), $(i+1)$	temporary value during iteration.

Subscripts

av	average value
b	bottom plate
c	cold plate
f	fluid
l	liquid
m	porous medium
m, n	grid point
s	solid particle
t	top plate
0	property at room temperature.

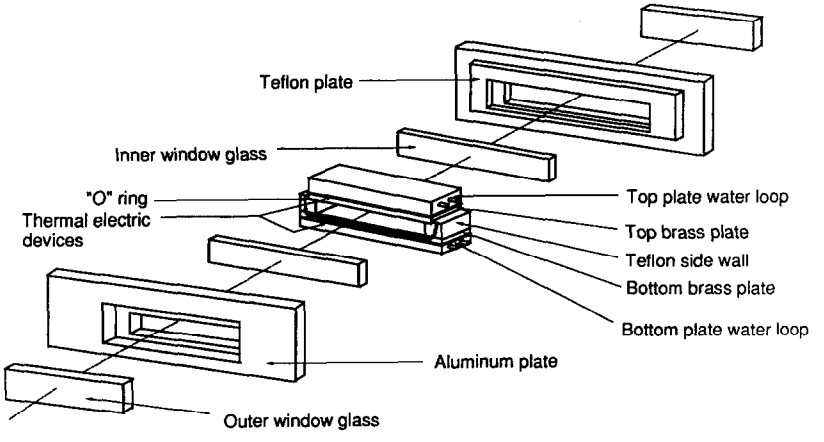

a

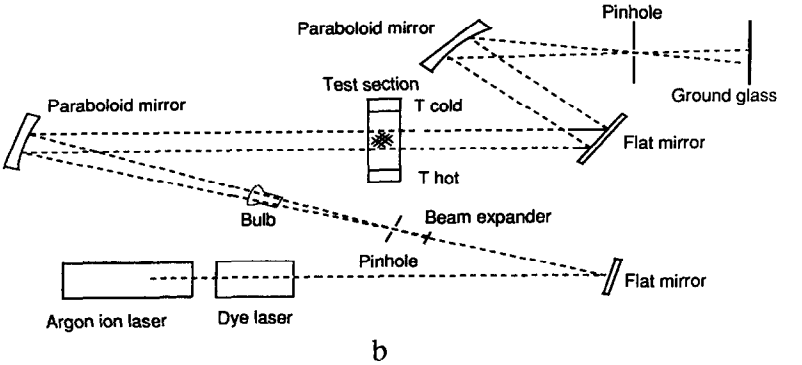

b

FIG. 1. Schematic diagrams of the experimental setup: (a) an exploded view of the test section; (b) a diagram of the optical setup.

the test section in this study were the following: length 54.6 cm; height 7.54 cm and width 4.78 cm. The choice of this geometry was based on the results obtained by Davis [8] for a single component flow—that the axis of the rolls will be parallel to the shortest side for a rectangular box. To reduce heat conduction, the side walls and inner surfaces of the front and back walls must be made of a material of low thermal conductivity. In addition, this material must resist attack by the organic fluid used in the study. Teflon was an ideal material. Each observing window (perpendicular to the optical path) was made of two glass plates (thermopane fashion). Dry nitrogen flow rate was very low between the two plates of each window to avoid vapor condensation when the temperature of the cold boundary (upper plate) was below the dew point temperature of the air. Hydrite was placed between the two glass plates of each window to absorb any condensed water vapor that may be present. The top and bottom brass plates (1.27 cm thick) were heated and cooled by two constant temperature water circulating loops. When the top and bottom plates reached steady state, the variation in surface temperature over each plate was less than 0.1°C. This was determined by sweeping the surface of the plates with a thermocouple when the test section was disassembled. Four stainless steel, thin wall tubes (0.075 cm outside diameter) were brazed into slots that were machined into the two surfaces of the top and bottom plates of the test section. Thermocouples, with thermal compound applied to their tips, were inserted into these stainless steel tubes after the test section was assembled. In this manner, one can measure the surface temperatures of the plates.

The porous medium in these experiments consisted of glass (sodalime) beads having a uniform index of refraction of approximately 1.51. Because of the manufacturing process, it was not possible to purchase beads below 3 mm in diameter having a uniform index of refraction. Although beads of approximately 3.0 mm or larger were used in previous studies [9, 10], we were interested in beads smaller than 3.0 mm in diameter because of their practical application. Thus, it was necessary to purchase a sheet of plate glass (Pittsburgh plate) and crush it—forming beads. These beads had to be sieved, cleaned and annealed. The annealing was necessary to remove residual stresses, otherwise there will be a non-uniformity in the index of refraction. No effort was made to assure that the beads were spherical. The thermal properties of the glass beads at room temperature were as follows: thermal conductivity, $k = 0.78$ W m^{-1} °C^{-1}; density, $\rho = 2700$ kg m^{-3}; specific heat, $C_p = 0.84$ kJ kg^{-1} °C^{-1}; and thermal diffusivity, $\alpha = 3.4 \times 10^{-7}$ m^2 s^{-1}.

The liquid used in these experiments was ethyl salicylate which has an index of refraction of 1.51 at room temperature. Its melting point is 2.5°C—which is ideal for the freezing experiments reported in Part II. There are however two other reasons which are important in the selection of this fluid. (1) This fluid is safe to work with—from a health hazard point of view. Chlorobenzene used by Klarsfeld [4] has the proper physical properties, but is a cancer suspect fluid. (2) Ethyl salicylate is readily available and its cost is not prohibitive. The thermal properties of this liquid at room temperature are $k = 0.155$ W m^{-1} °C^{-1}; $\rho = 1310$ kg m^{-3}; $\nu = 2.77$ centipoise.

When assembling the test section prior to the tests, care was taken to remove air bubbles. Otherwise the trapped bubbles would yield non-reproducible, and erroneous results. Since the bubbles are clearly visible in the test section, they can easily be expelled by carefully stirring the bed before positioning the top plate.

Two light sources were used to visualize the isotherms generated by the Christiansen effect. One source, an argon ion laser in conjunction with a dye laser, was used for quantitative measurements. The argon ion laser was operated in the multi-wavelength mode with two dominant wavelengths—5145 Å (green) and 4880 Å (blue). When the tunable dye laser was incorporated, it provided a monochromatic light source that spanned the wavelength range from 5680 to 6600 Å. The wavelength drive of the dye laser was calibrated using a monochromator. Further calibration relating wavelength to temperature, was achieved as follows: by cooling the bottom plate and heating the top plate, pure conduction (linear temperature profile) is established in the test section. The plate temperatures (top surface of bottom plate and bottom surface of top plate) were measured with thermocouples. Knowing the temperature distribution allows one to relate wavelength to temperature. The other light source used was an incandescent lamp. This has the advantage of simultaneously providing a full range of wavelengths in the visible spectrum. Thus, it provides global information about the temperature field and is excellent for demonstration purposes. However, since this light source is not parallel, it was not used for quantitative measurements.

Figure 1(b) is a schematic drawing of the optical setup used in this experiment. Since it was important for quantitative measurements (laser light source) that the incident light be parallel, a pin hole assembly in conjunction with an off-axis parabolic mirror was used. With this setup the solid angle of the incoming beam is approximately 10^{-8} sr. For the receiving optics, a folding mirror and a parabolic mirror were used to focus the parallel light that passes the test section through a pin hole. An image of the test section is focused on a ground glass surface. The solid angle of the receiving optics is approximately 5×10^{-8} sr. According to Cloupeau and Klarsfeld [11], this provides a half bandwidth of less than 20 Å for each of the laser wavelengths—which is excellent resolution. A video camera was used to record the output. For quantitative measurements (laser light source), a software program termed 'image processor' was used to identify the isotherms (lines of maximum intensity).

In the digitized image, there are 125 pixels that extend from the bottom plate to the top plate of the test section (5.08 cm). Thus the spatial resolution after using the image processor is 0.04 cm. In the convection region, where the temperature gradient is relatively small, the temperature resolution is better than 0.2°C. For the incandescent light source used in global observations, pictures of the test section were taken and recorded with a video camera, VCR and color monitor. In these observations, the receiving optics were not used—the pattern observed was from scattered light (not parallel light) that penetrated the test section.

Since the physical size of the light source is limited by the size of the off-axis parabolic mirror used in the transmitting optics (12.7 cm), one could not observe the entire horizontal extent of the test section at any one instant. This difficulty was resolved by placing the test section on rails with Thompson bearings; thus, the test section could be slowly (and smoothly) moved horizontally in a plane perpendicular to the laser beam without disturbing the flow. Except when freezing initially occurs (which will be covered in Part II), the time scales are long compared to the time required to collect the data over the entire test section. Thus, it was possible to take multiple pictures covering the entire test section—including some overlap in each frame. Composite pictures are used to display the experimental data.

The control parameter in this porous system is the modified Rayleigh number (Ra) defined as $Ra = Kg\beta\Delta TH/\nu\alpha$. Since the permeability (K), thermal expansion coefficient (β) and thermal diffusivity (α) are not readily available, their combined values, ($K\beta/\alpha$), were determined as follows: by observing the isotherm pattern, it was possible to establish the critical condition (onset of instability) in the test section by carefully varying the temperatures on the top and bottom plates. Since this critical Rayleigh number is well defined (equal to $4\pi^2$), the quantity $Kg\beta H/\nu\alpha$ is treated as a lumped constant independent of temperature. For each run of the experiment, the modified Rayleigh number was determined by the product of this constant and temperature difference across the boundaries.

THEORETICAL FORMULATION

Although others [2, 6, 12] have reported numerical solutions to this problem, a numerical program was developed so that one could obtain results that match the experiments over a wide range of operating conditions. In particular, the temperature dependence of the liquid viscosity is included. The computational domain is a two-dimensional rectangular space of height H and horizontal dimension L filled with a porous medium of permeability K.

The governing equations are the usual ones with the momentum equation replaced by Darcy's law:

$$\frac{\partial U}{\partial X}+\frac{\partial V}{\partial Y}=0 \tag{1a}$$

$$\frac{\mu U}{K}=-\frac{\partial P}{\partial X} \tag{1b}$$

$$\frac{\mu V}{K}=-\left(\frac{\partial P}{\partial Y}+\rho g\right) \tag{1c}$$

$$U\frac{\partial T}{\partial X}+V\frac{\partial T}{\partial Y}=\alpha\left(\frac{\partial^2 T}{\partial X^2}+\frac{\partial^2 T}{\partial Y^2}\right) \tag{1d}$$

where U and V are area averaged velocities; P, μ, and T are porous medium pressure, viscosity, and temperature, respectively. The parameter α is the effective thermal diffusivity of the porous medium and is defined as $\alpha = k_m/(\rho C_p)_f$ where k_m is the thermal conductivity of the porous medium and subscript f denotes the properties of the liquid.

The Boussinesq approximation is assumed; that is, the temperature dependence of density is maintained as the driving force in the momentum equation, but is constant in the conservation of energy and mass equations. It is convenient to eliminate P by cross differentiation and introducing $\rho = \rho_0(1-\beta(T-T_0))$ in the buoyancy term. The temperature dependence of viscosity is incorporated by introducing a nondimensionalization factor f; that is

$$f=f(T)=\frac{\nu(T)}{\nu_0(T_{av})}=\frac{\mu/\rho}{\mu_0/\rho_0}. \tag{2}$$

The kinematic viscosity of the ethyl salicylate was measured with an Ostwald viscometer and found to be

$$\nu(T)=6.73-1.32\ln(T)-5.5\times10^{-6}(T-37.8)+10^{-4}(T-37.8)\ln(T) \tag{3}$$

where T is in °C and ν is in centipoise.

Thus the following momentum equation, based on Darcy's law, is obtained:

$$\frac{\partial}{\partial Y}(fU)-\frac{\partial}{\partial X}(fV)=\frac{-Kg\beta\rho_0}{\nu_0}\frac{\partial T}{\partial X}. \tag{4}$$

The stream function was introduced and all the variables are nondimensionalized as follows:

$$\hat{X}=\frac{X}{H},\quad \hat{Y}=\frac{Y}{H},\quad \hat{\psi}=\frac{\psi}{\alpha},\quad \hat{T}=\frac{T-T_C}{T_H-T_C}. \tag{5}$$

Equations (1) can be rewritten as

$$\frac{\partial}{\partial\hat{X}}\left(f\frac{\partial\hat{\psi}}{\partial\hat{X}}\right)+\frac{\partial}{\partial\hat{Y}}\left(f\frac{\partial\hat{\psi}}{\partial\hat{Y}}\right)=-\frac{Kg\beta\Delta TH}{\alpha\nu_0}\frac{\partial\hat{T}}{\partial\hat{X}}=-Ra\frac{\partial\hat{T}}{\partial\hat{X}} \tag{6a}$$

$$\frac{\partial^2\hat{T}}{\partial\hat{X}^2}+\frac{\partial^2\hat{T}}{\partial\hat{Y}^2}=\frac{\partial\hat{\psi}}{\partial\hat{Y}}\frac{\partial\hat{T}}{\partial\hat{X}}-\frac{\partial\hat{\psi}}{\partial\hat{X}}\frac{\partial\hat{T}}{\partial\hat{Y}}. \tag{6b}$$

The corresponding dimensionless boundary conditions are

$$\hat{T}=0 \text{ at } \hat{Y}=1$$

$$\hat{T} = 1 \text{ at } \hat{Y} = 0$$

$$\frac{\partial \hat{T}}{\partial \hat{X}} = 0 \text{ at } \hat{X} = 0 \text{ and } \hat{X} = \frac{L}{H} = A$$

$\hat{\psi} = 0$ on all walls for the impermeable case

$\hat{\psi} = 0$ at $\hat{X} = 0$, A and $\hat{Y} = 0$ and

$$\left.\frac{\partial \hat{\psi}}{\partial \hat{Y}}\right|_{\hat{Y}=1} = U = 0 \text{ for the permeable case.} \quad (7)$$

For the permeable case, pressure was assumed to be constant at the upper boundary of the porous layer. Thus from Darcy's law the horizontal velocity is equal to zero. The boundary temperature at the porous layer interface was assumed to be constant and determined from the measured heat flux at the top plate and the assumed linear temperature profile in the liquid layer. In reality, the temperature distribution along the interface has a sinusoidal type distribution whose amplitude depends on the convection rolls in the porous layer [13]. In the present case, the temperature variation may be as large as 10°C at the highest modified Rayleigh number. Since the liquid layer is very thin compared to the porous layer, the flow field in the liquid layer was neglected.

The finite difference method was employed in the numerical simulation. The upwind difference method [14] was used in equation (6b) to discretize the convection term, and the central difference method was used to discretize the Laplacian terms (equations (6a) and (6b)). The reason for choosing the upwind difference method was to ensure numerical stability. This can avoid the non-convergent results in Elder's [9] work at high Ra flow. In choosing the mesh size, some numerical experiments were conducted to compare accuracy and computational time. A 41×41 mesh was found to be reasonably accurate and economic in computational time. Equations (6) were solved by using the successive over relaxation (SOR) method with the given boundary conditions (equation (7)). The relaxation factor was chosen as 1.3. This factor depends on mesh size, shape of domain, and types of boundary conditions. For the Newman condition (in the present case), there is no analytical solution for the optimal relaxation factor [15]. Therefore, numerical experiments were performed to determine the relaxation factor that yielded the highest convergent rate. Thus the value of 1.3 was chosen. The temperature profile and the stream function converged with a relative error of 10^{-5}, which is defined as

$$E_{rr} \equiv \sqrt{\left(\frac{\sum_{m,n} |(Q_{m,n}^{(i+1)} - Q_{m,n}^{(i)})/R|^2}{\sum_{m,n} |Q_{m,n}^{(i)}|^2}\right)} \quad (8)$$

where $Q_{m,n}^{(i)}$ is either $\hat{T}$ or $\hat{\psi}$ in equations (6a) and (6b); R is the relaxation factor.

The computational procedure begins with an initial guess of the isotherm profile and stream function. This initial guess can be approximated by a sinusoidal function. Since there exist multiple solutions for this set of governing equations, the choice of the initial guess relies heavily on the experimental results—especially with regard to wave number. Equation (6b) is solved for $\hat{T}$ by substituting an intial guess of $\hat{\psi}$ with boundary conditions. Then the computed $\hat{T}$ is substituted in equation (6a) and $\hat{\psi}$ is computed which also satisfies the boundary conditions. Iterations are continued until the convergence criterion is fulfilled. After $\hat{T}$ and $\hat{\psi}$ are computed, the local and average Nusselt number can be calculated.

EXPERIMENTAL RESULTS

In these experiments, the top plate temperature was usually maintained at a fixed temperature and the bottom plate temperature was increased in ~5°C increments. Since the permeability depends heavily on bead size, 2.5 mm beads were used in these experiments to maintain reasonably high Rayleigh numbers within the heating and cooling capacity of the water loops. For each temperature setting between 2 and 3 h is allowed to assure the system reaches steady state.

Figure 2(a) shows a typical picture taken with the incandescent light as the light source. This picture clearly demonstrates what is meant by global temperature field. A black and white photograph does not do justice to the color photograph where the bands of colors range from blue to red and are clearly seen. Only one band (yellow) is seen in the black and white photographs. As stated earlier this picture was taken by directly focusing on the test section and bypassing the receiving optics. The global temperature pictures were taken at an angle approximately 20 deg from the optical axis. Since the incandescent light source is not parallel light and since the receiving optics are bypassed, the light that penetrates the test section is scattered light. Figure 2(b) is a corresponding picture taken with the laser beam as the light source and receiving optics in place. This picture was taken with the dye laser output set at 5601 Å (26.0°C) and recorded with a video camera. Data from the VCR are analyzed using an image processor software which selects values of maximum intensity and digitizes the results; as described earlier. The width of the bright laser band in Fig. 2(b) covers three pixels; thus the width of the isotherm obtained from this figure will be reduced by a factor of three.

Figure 3 shows a sequence of pictures of the global temperature field with increasing modified Rayleigh numbers. Figure 3(a) is taken at $Ra = 39.9$ which is slightly above the critical modified Rayleigh number. The isotherms are nearly straight. As the modified Rayleigh number is increased to $Ra = 45.4$, the isotherms begin to undulate and are approximately sinusoidal in shape (see Figs. 3(b) and (c)). With a further increase in the modified Rayleigh number, the isotherms deform further and begin deviating from a sinusoidal shape. The modified Rayleigh number was increased until a value of 72.3 was reached. This cor-

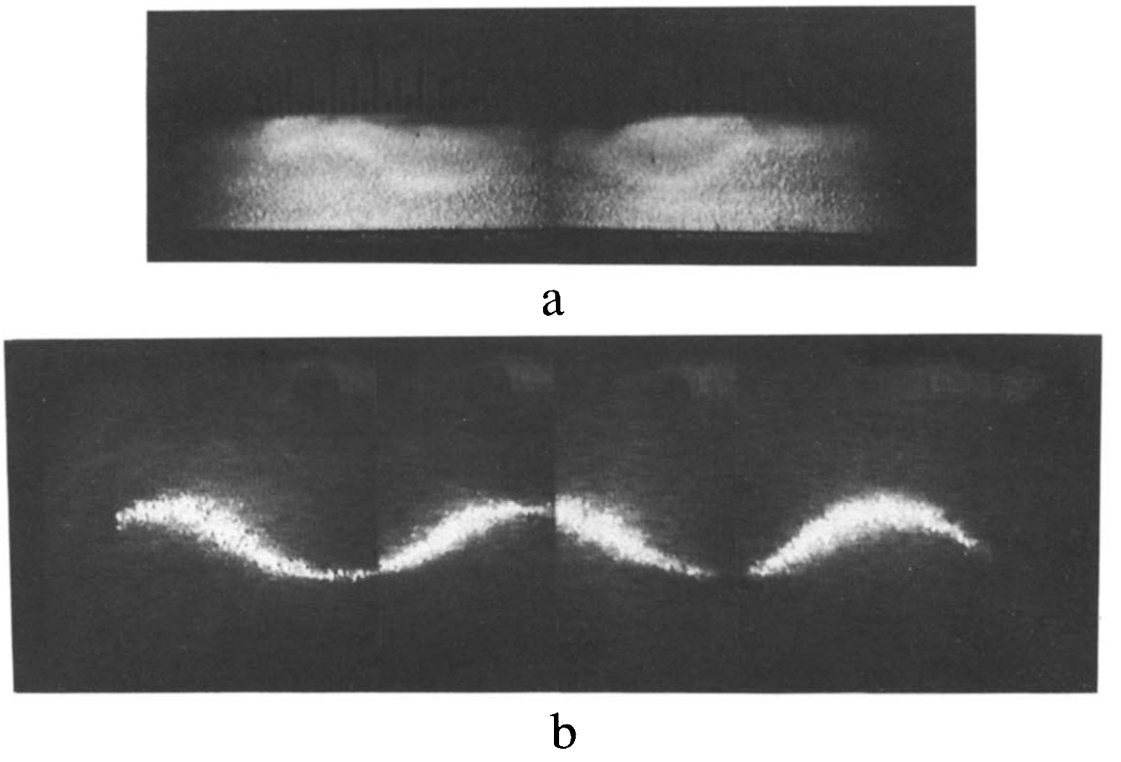

FIG. 2. Photographs of the temperature field where $Ra = 51$ ($T_t = 3.2°C$ and $T_b = 55°C$): (a) a photograph of the global temperature field; (b) a photograph of a laser light source—5601 Å, corresponding to 26°C.

responds to a top plate temperature of 2.8°C and bottom plate temperature of 69.5°C. These are the limits of the circulating constant temperature baths. One could have increased the depth of the test section to further increase *Ra* (*Ra* varies linearly with depth), but this would have reduced the aspect ratio of the test section. The experiments conducted are within the stable finite amplitude mode. Unstable behavior of convective cells in a porous medium occurs when the modified Rayleigh number exceeds 380 [16]. Later when comparing experiments with numerical calculations, the isotherms obtained using the laser as a light source will be shown.

The isotherm pattern strongly depends on the boundary conditions in the experimental setup. In Fig. 3, care was taken to insure the glass beads were in direct contact with the top plate. This was done by filling the test section with beads and fluid to a level slightly above the supports on which the top plate sat. The top plate was then carefully positioned on the porous bed. Figure 4 is an example of the early experiments that were conducted where the isotherms lacked symmetry about the midplane as seen in the previous figures. In addition, these earlier experiments were not reproducible. This test, shown in Fig. 4, was conducted at approximately the same plate temperatures as those in Fig. 3(f). This failure to obtain reproducibility and symmetry was initially confusing. It was believed that the test section was completely filled with the porous bed. However, on careful examination of the global pictures with the VCR, a very thin layer of fluid approximately 0.05 cm deep (without beads) was detected at the top plate. This thin layer, not of uniform thickness, can be seen in Fig. 4 (much more clearly seen on the color photograph) and was the cause of the asymmetry and non-reproducible results. Each time the test section was refilled, different regions of the liquid layer—devoid of beads—were in contact with the upper plate. This thin layer changes the hydrodynamic boundary from an impermeable layer to a permeable layer over portions of the top boundary. This, in turn, causes a significant effect on the entire temperature (and flow) pattern. Chandrasekhara and Munchen [17], discussed the effect of non-uniform permeability near the top plate and found the results on the flow field to be significant. To investigate this boundary effect in greater detail, a uniform liquid layer 0.8 cm deep was imposed between the beads and the top plate. When the experiments were repeated, one obtained the very asymmetric but reproducible isotherm patterns. In these tests involving a permeable upper boundary, there is a difference in the number of rolls in the test section from those that appear with an impermeable boundary. That is, the cell width changes. In the case of the impermeable boundary condition there are eight rolls in the test section (Fig. 3); in the case of the permeable boundary there are six rolls in the test section.

One problem investigated by researchers in the past has been the variation in the cell size as a function of modified Rayleigh number. In our experiments, the spacing of the cells (width/height) increases with

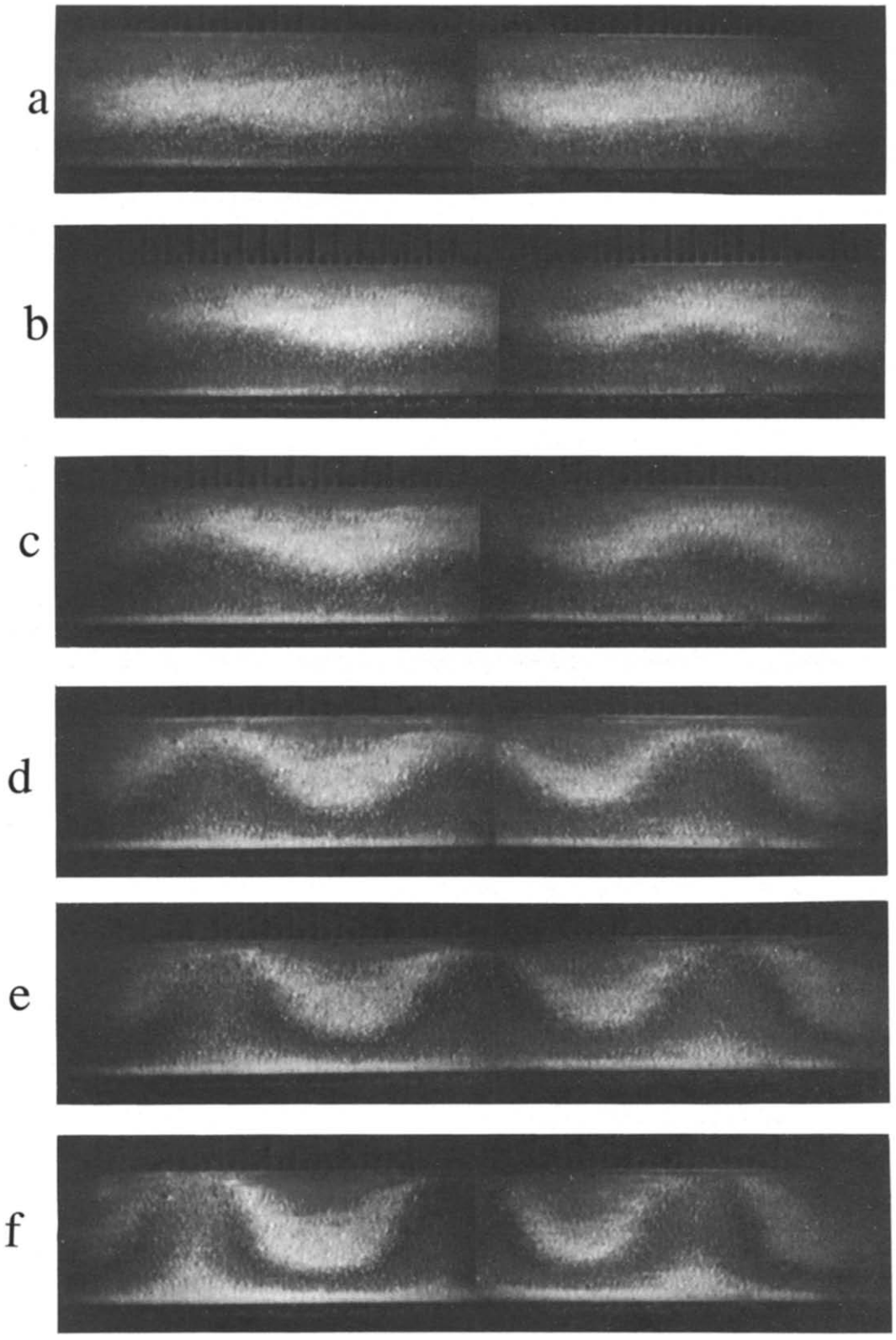

FIG. 3. Photographs of the global temperature fields for impermeable boundary condition at different Rayleigh numbers: (a) $Ra = 39.9$, $T_t = 2.4°C$, $T_b = 44.2°C$; (b) $Ra = 45.4$, $T_t = 2.6°C$, $T_b = 50°C$; (c) $Ra = 51.4$, $T_t = 2.7°C$, $T_b = 55.5°C$; (d) $Ra = 58.3$, $T_t = 2.6°C$, $T_b = 60.5°C$; (e) $Ra = 64.2$, $T_t = 2.7°C$, $T_b = 64.5°C$; (f) $Ra = 72.3$, $T_t = 2.8°C$, $T_b = 69.5°C$.

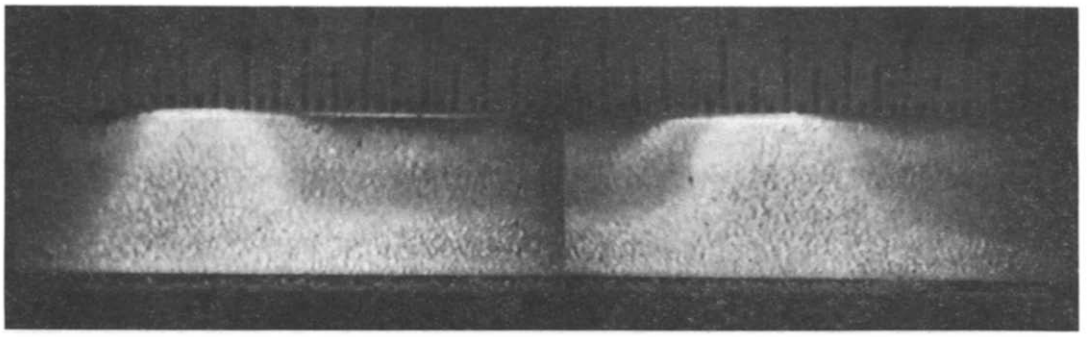

FIG. 4. Photograph of the global temperature field where the upper boundary is permeable. $Ra = 70.4$ and the liquid layer at the top plate is approximately 0.05 cm deep.

increase in modified Rayleigh number for a permeable upper boundary. In these experiments there were initially six rolls in the test section (Ra slightly above Ra_{crit}) which were uniformly positioned. As the modified Rayleigh number increases, the width/height ratio of the roll increased. Due to the finite width of the test section, the width/height measurements were made on the centrally located cells. From the many experiments that were performed, these results are reproducible. The numerical solution, however, does not yield a change in cell spacing with Rayleigh number. A possible explanation may be the simplifying assumptions in the numerical simulation that the pressure and temperature are constant along the interface. For the case of the impermeable upper boundary, the cell size does not change over the range of modified Rayleigh numbers in these experiments. This result is summarized in Fig. 5(a). To further investigate this subject, the aspect ratio of the test section was changed (from 6.04 to 12.5) by decreasing the depth of the test section. The bead size was also varied—1, 2.5, 5 mm. Figure 5(b) shows the cell size does not change over the range of the modified Rayleigh numbers in our experiments, regardless of the bead size and aspect ratio of the test section for the impermeable top boundary. These experimental results contradict Combarnous and Bories' result [5] which states that the cell width/height ratio decreases with an increase in modified Rayleigh number.

COMPARISON BETWEEN EXPERIMENTS AND NUMERICAL SIMULATIONS

Figure 6 shows the calculated values and the experimental values of the isotherms corresponding to the experimental conditions of Fig. 3. To avoid cluttering the plot, only three (18.6, 26.0, 38.2°C) of the six experimentally determined isotherms are plotted for comparison. The agreement is generally good. The discrepancies are believed to be due to the uncertainties in determining the modified Rayleigh numbers, non-spherical beads, and the non-uniformity of size of the glass beads within the sieving process. These data are for impermeable boundary conditions. It is noted that there are eight rolls in the test section in both the computed values and the experiments. The streamline plots of Fig. 6 show the convective flow direction. From left to the right, the sign of odd rolls is negative and that of the even rolls is positive. The stream function definition indicates the flow direction of odd rolls is clockwise and even rolls is counterclockwise. This results in the downward movement of cold fluid and upward movement of hot fluid which appear in the corresponding isotherm plots.

Figure 7 shows the numerical simulation and experimental results for a permeable upper boundary—the superposed liquid layer is 0.8 cm deep. Agreement between theory and experiments is reasonably good at low Rayleigh numbers (Figs. 7(a) and (b)). However, the cell width/height ratio increases with Rayleigh number in the experiments—but not in the numerical calculations. This leads to a divergence between the experimental results and the numerical calculations at higher Rayleigh numbers (Figs. 7(c) and (d)). Nevertheless the overall characteristic shape of the experimentally determined isotherms agrees with those numerically determined. That is, the peaks are narrow and the troughs are broad. The streamline plots indicate the streamlines become vertical at the permeable boundary which means no horizontal flow at the interface [2]. It should be noted that the number of rolls in the test section in this case is six—in both the experiments and the numerical simulations.

From the numerical solution, the local Nusselt numbers at the upper and bottom plates can be calculated. Typical results are shown in Fig. 8 for a particular Rayleigh number. Where both boundary conditions are impermeable, the curves are symmetric and out of phase in the space coordinate (Fig. 8(a)). For the case of a permeable boundary (see Fig. 8(b)), the plots of Nusselt numbers are not symmetric; the top plate Nusselt number is much greater in magnitude than the bottom plate Nusselt number. These results are expected because there is less resistance at the upper boundary for the permeable case. One can also see a significant increase in the magnitude of the local Nusselt number at the bottom plate for the permeable case as compared to the impermeable case. The increase in resistance to flow at the upper plate

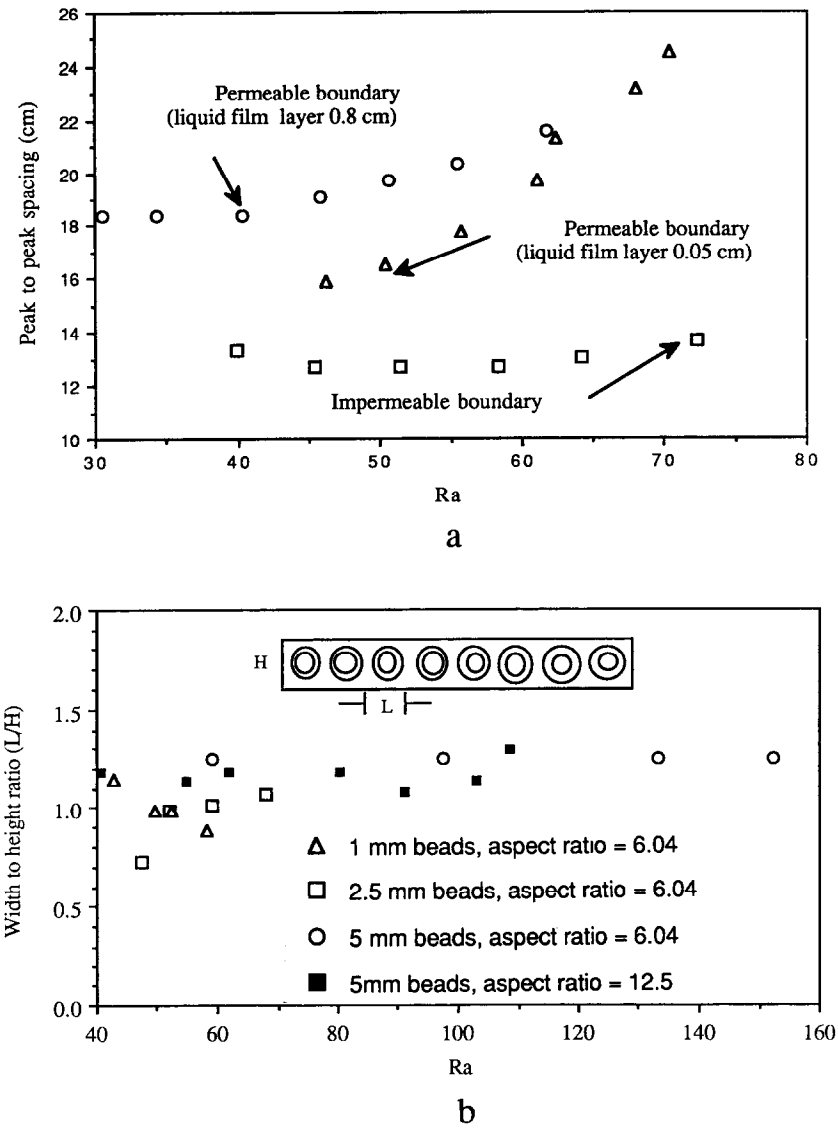

FIG. 5. Spacing and width to height ratios for cells with permeable and impermeable boundaries as a function of Rayleigh number: (a) the effect of permeability on cell spacing; (b) the effect of test section aspect ratio and bead size on cell width to height ratio.

for the impermeable case has its effects felt throughout the flow.

Figure 9 contains plots of Nusselt number vs Rayleigh number obtained by various researchers; as well as the numerical results of this study. Buretta and Berman's [10] correlation for $0 < Ra < 100$ is shown, which is within the range of the experiments and numerical calculations in this study. It is noted that Buretta and Berman's data have a slope that is similar to our numerical results but yield significantly larger Nusselt numbers. However, since their experiments were performed in a circular test section—not rectangular (as in our case), it is expected that their results would be different. The majority of Elder's experiments [9] were also conducted in a circular test section using glass beads of diameters 3, 5, 8 and 18 mm. These data, he concludes, follow the curve $Nu = Ra/40$. Holst and Aziz [1] determined a relation between Nusselt number and Rayleigh number numerically. Their results are seen to lie significantly above our results; as well as those of other researchers. These results were obtained using n-heptane as the fluid, and included the temperature dependence of the physical properties—density, specific heat, and viscosity. Holst and Aziz varied the Rayleigh number by changing the permeability of the medium; we varied the Rayleigh number by changing the top and bottom plate temperatures—as in the experiments. This difference, however, should not be relevant. In our analysis we included the temperature dependence of the viscosity of ethyl salicylate. Our only explanation for this discrepancy is that the physi-

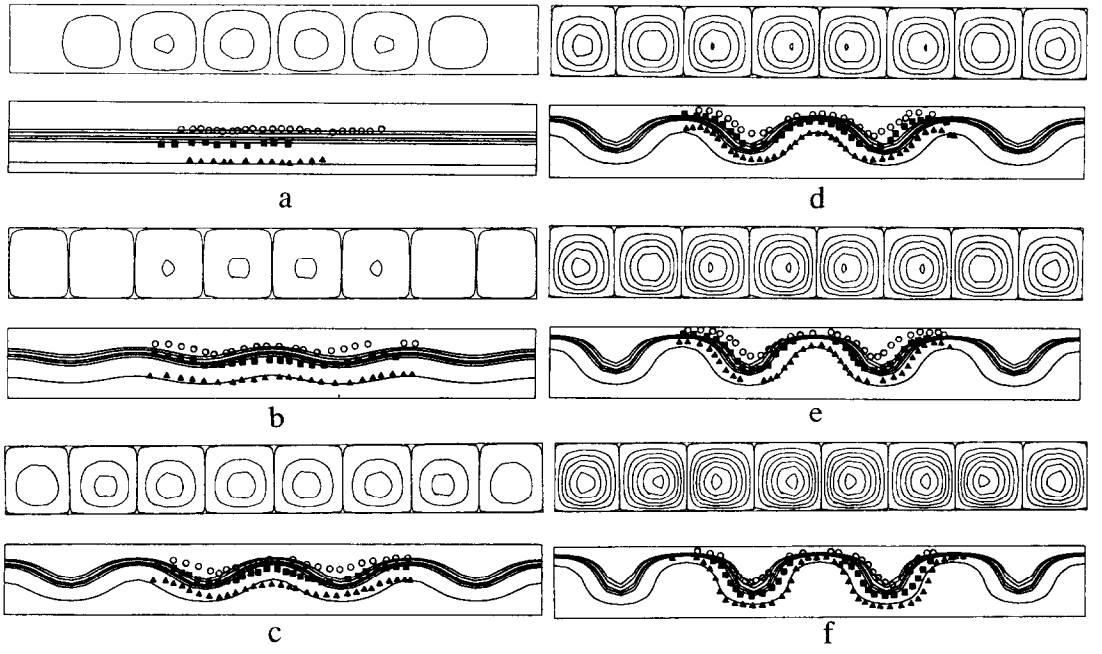

FIG. 6. Plots comparing the numerical and experimental results for impermeable boundaries: (a) $Ra = 39.9$; (b) $Ra = 45.4$; (c) $Ra = 51.4$; (d) $Ra = 58.3$; (e) $Ra = 64.2$; (f) $Ra = 72.5$. The theoretical isotherms (solid lines) are as follows: 18.6, 20.5, 22.6, 24.1, 26 and 38.2°C. The experimental isotherms—18.6, 26, and 38.2°C are represented by ○, ■, and ▲, respectively. Streamlines are also shown.

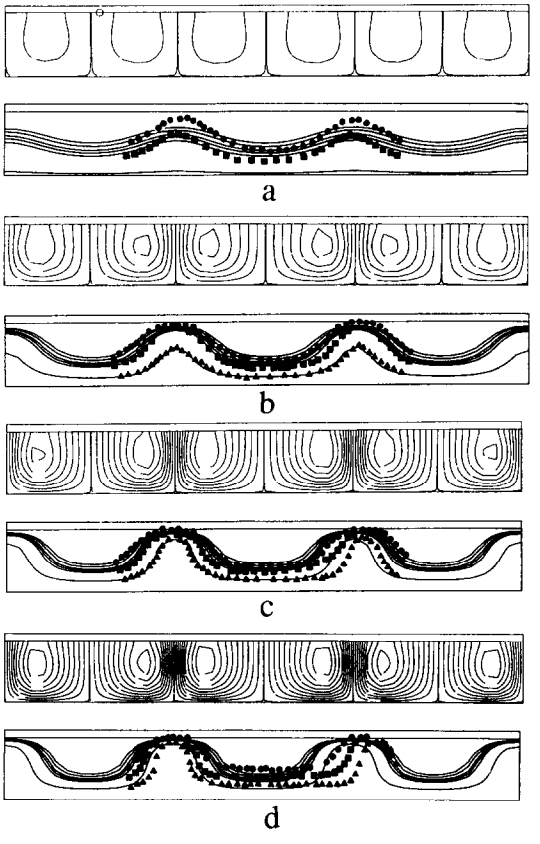

FIG. 7. Plots comparing the numerical and experimental results for the permeable top boundary: (a) $Ra = 30.6$; (b) $Ra = 40.3$; (c) $Ra = 50.7$; (d) $Ra = 61.7$. The theoretical isotherms (solid lines) are as follows: 18.6, 20.5, 22.6, 24.1, 26 and 38.2°C. The experimental isotherms—18.6, 26, and 38.2°C are represented by ●, ■, and ▲, respectively. Streamlines are also shown.

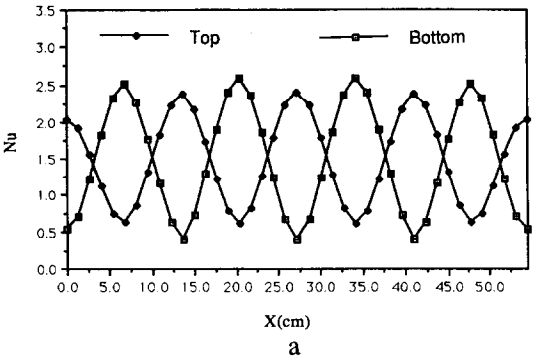

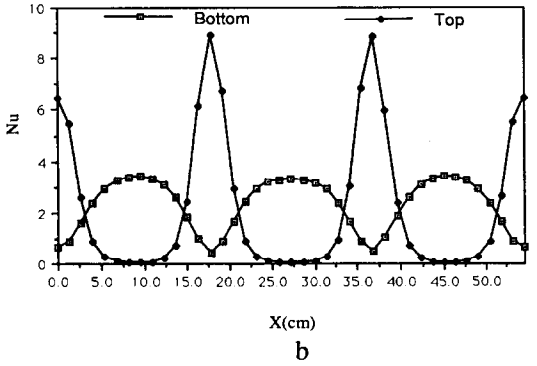

FIG. 8. Plot of local Nusselt number along top and bottom boundaries: (a) plot where the top plate is impermeable and $Ra = 64.2$; (b) plot where the top plate is permeable and $Ra = 61.7$.

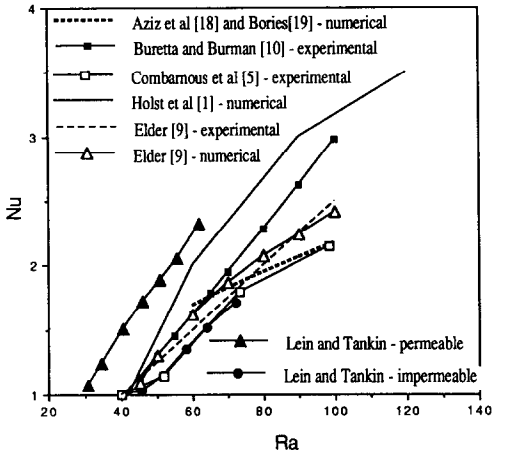

FIG. 9. Plot of the average Nusselt number at the bottom plate vs Rayleigh number.

cal properties of n-heptane are much different than those of ethyl salicylate. Later, Aziz and Combarnous [18] and Bories [19] obtained the relation $Nu = 0.218(Ra)^{1/2}$ over the Rayleigh number range (60–4000). This relation, obtained using the power integral method, is plotted in Fig. 9 and seen to lie above our numerical values in the small region of overlap. Also seen in Fig. 9 are the experimental results presented by Combarnous and Bories [5] for glass beads of 3 mm in diameter in water and 1.9 mm glass beads in oil. These results are in close agreement with our numerical computations. Finally, included in Fig. 9 are our numerical results for a permeable top plate. This is included because all the data lies between the permeable and impermeable (top plate) numerical values of this study. If there is a thin layer (or partial layer) of liquid inadvertently located at the top plate in one's experiments, it can have a large effect on the relationship between Nusselt number and Rayleigh number.

CONCLUSIONS

The experimental setup gave excellent resolution of the isotherms in the test section. These experiments were conducted without disturbing the flow and they agreed with the numerical calculations. In our experiments, the aspect ratio of the cell—cell height/cell width—for the impermeable boundaries did not vary with modified Rayleigh number as predicted by others; such as Combarnous. For a permeable upper boundary case, the aspect ratio of the cell decreased with an increase in modified Rayleigh number. Local Nusselt numbers for the top and bottom plates were computed and presented.

Acknowledgements—The authors wish to thank the National Science Foundation for support of this study. This study was supported under grant number MEA8405128.

REFERENCES

1. P. H. Holst and K. Aziz, A theoretical and experimental study of natural convection in a confined porous medium, *Can. J. Chem. Engng* **50,** 232 (1972).
2. R. J. Ribando and K. E. Torrance, Natural convection in a porous medium: effects of confinement, variable permeability and thermal boundary condition, *J. Heat Transfer* **98,** 42 (1976).
3. H. H. Bau and K. E. Torrance, Low Rayleigh number thermal convection in a vertical cylinder filled with porous medium and heated from below, *J. Heat Transfer* **104,** 166 (1982).
4. S. M. Klarsfeld, Champs de Temperature Associes aux Mouvements de Convection Naturelle dans un Milieu Porous Limite, *Revue Gen. Thermique* **108,** 1403 (1970).
5. M. Combarnous and S. A. Bories, Hydrothermal convection in saturated porous medium, *Adv. Hydrosci.* **10,** 231 (1975).
6. A. Bejan, *Convection Heat Transfer*, p. 343. Wiley, New York (1984).
7. R. Farhadieh and R. S. Tankin, Interferometric study of two-dimensional Bénard convection cells, *J. Fluid Mech.* **66,** 739 (1974).
8. S. H. Davis, Convection in a box: linear theory, *J. Fluid Mech.* **30,** 465 (1967).
9. J. W. Elder, Steady free convection in a porous medium heated from below, *J. Fluid Mech.* **27,** 29 (1976).
10. R. J. Buretta and A. S. Berman, Convective heat transfer in a liquid saturated porous layer, *J. Appl. Mech.* **98,** 249 (1976).
11. M. Cloupeau and S. Klarsfeld, Visualization of thermal fields in saturated porous media by the Christiansen filter effect, *Appl. Optics* **12**(2), 198 (1973).
12. T. W. Tong and S. Orangi, A numerical analysis for high modified Rayleigh number natural convection in

enclosure containing a porous medium, *Int. Heat Transfer Conf.*, San Diego (1986).
13. H. Lein, Natural convection in porous media, Ph.D. Thesis, Northwestern University, p. 153 (1990).
14. S. V. Patankar, *Numerical Heat Transfer and Fluid Flow*, p. 83. Hemisphere, Washington, DC (1980).
15. P. J. Roache, *Computational Fluid Dynamics*, p. 118. Hermosa, Albuquerque (1976).
16. J. M. Straus, Large amplitude convection in porous medium, *J. Fluid Mech.* **64,** 51 (1974).
17. B. C. Chandrasekhara and D. Munchen, Vortmeyer flow model for velocity distribution in fixed porous medium bed under isothermal conditions, *Wärme- und Stoffübertragung* **12,** 105 (1979).
18. K. Aziz and M. Combarnous, Prédiction théorique du transfert de chaleur par convection naturelle dans une couche poreuse horizontale, *C. r. Acad. Sci. Sér. B* **271,** 813 (1970).
19. S. A. Bories, Comparaison des prévisions d'une théorie non linéaire et des résultats expérimentaux en convection naturella dans une couche poreuse saturée horizontale, *C. r. Acad. Sci. Sér. B* **271,** 269 (1970).

CONVECTION NATURELLE DANS LES MILIEUX POREUX—I. PAS DE CONGELATION

Résumé—Le concept de filtre de CHRISTIANSEN est utilisé pour visualiser la convection naturelle dans les milieux poreux. Des études sont conduites pour des frontières supérieures perméable et imperméable. Les résultats expérimentaux s'accordent bien avec les calculs numériques basés sur la loi de DARCY. Trois perméabilités différentes et différents rapports de forme de la section d'essais (largeur/hauteur) sont examinés. On trouve que le rapport de forme des cellules ne varie pas avec le nombre de RAYLEIGH modifié pour la frontière supérieure imperméable, mais ce rapport augmente sensiblement avec ce nombre pour la frontière supérieure perméable.

NATÜRLICHE KONVEKTION IN PORÖSEN MEDIEN—I. OHNE GEFRIEREN

Zusammenfassung—Die natürliche Konvektion in porösen Medien wird mit Hilfe des Filterverfahrens nach Christiansen sichtbar gemacht. Es werden Untersuchungen mit durchlässiger und mit undurchlässiger oberer Grenzfläche durchgeführt. Die experimentellen Ergebnisse stimmen gut mit numerischen Berechnungen auf der Grundlage des Darcy'schen Gesetzes überein. Die Untersuchungen umfassen drei unterschiedliche Permeabilitäten sowie unterschiedliche Seitenverhältnisse (Breite/Höhe) der Meßstrecke. Es zeigt sich, daß das Seitenverhältnis bei undurchlässigen Grenzflächen sich nicht mit der modifizierten Rayleigh-Zahl verändert. Im Falle der durchlässigen oberen Fläche steigt dieses Verhältnis dagegen stark mit der modifizierten Rayleigh-Zahl an.

ЕСТЕСТВЕННАЯ КОНВЕКЦИЯ В ПОРИСТЫХ СРЕДАХ—I. ОТСУТСТВИЕ ЗАМОРАЖИВАНИЯ

Аннотация—Для визуализации естественной конвекции в пористых средах используется понятие фильтра Кристиансена. Исследования проводятся со средами, имеющими как проницаемые, так и непроницаемые границы. Экспериментальные данные хорошо согласуются с результатами численных расчетов на основе закона Дарси. Рассматриваются три случая различных проницаемостей и три значения отношения сторон (ширина/высота) экспериментального участка. Найдено, что величина отношения сторон ячеек не изменяется с изменением значения модифицированного числа Рэлея в случае непроницаемой верхней границы, но значительно увеличивается с ростом значения модифицированного числа Рэлея, когда верхняя граница является проницаемой.